Arterial Stiffness: Different Metrics, Different Meanings

B. Spronck
Department of Biomedical Engineering,
Yale University,
New Haven, CT 06520

J. D. Humphrey[1]
Fellow ASME
Department of Biomedical Engineering,
Yale University,
New Haven, CT 06520;
Vascular Biology and Therapeutics Program,
Yale School of Medicine,
New Haven, CT 06520
e-mail: jay.humphrey@yale.edu

Findings from basic science and clinical studies agree that arterial stiffness is fundamental to both the mechanobiology and the biomechanics that dictate vascular health and disease. There is, therefore, an appropriately growing literature on arterial stiffness. Perusal of the literature reveals, however, that many different methods and metrics are used to quantify arterial stiffness, and reported values often differ by orders of magnitude and have different meanings. Without clear definitions and an understanding of possible inter-relations therein, it is increasingly difficult to integrate results from the literature to glean true understanding. In this paper, we briefly review methods that are used to infer values of arterial stiffness that span studies on isolated cells, excised intact vessels, and clinical assessments. We highlight similarities and differences and identify a single theoretical approach that can be used across scales and applications and thus could help to unify future results. We conclude by emphasizing the need to move toward a synthesis of many disparate reports, for only in this way will we be able to move from our current fragmented understanding to a true appreciation of how vascular cells maintain, remodel, or repair the arteries that are fundamental to cardiovascular properties and function. [DOI: 10.1115/1.4043486]

Keywords: aorta, stress, atomic force microscopy, pulse wave velocity, elasticity

Introduction

Mechanical factors have long been known to play vital roles in arterial health, disease, and treatment. Studies dating back to the late 19th century showed that altered blood flow and pressure typically result in changes in luminal radius and wall thickness [1,2], thus foreshadowing the need to quantify the mechanoregulation of arterial structure and function. It was not until the 1970s, however, that it was discovered how such changes occur. Experiments on cultured endothelial cells and vascular smooth muscle cells revealed flow- and stretch-induced changes in secreted proteins that resulted from altered gene expression [3,4]. Hence was born the field of vascular mechanobiology, reviews of the first three decades of which can be found elsewhere [5,6]. Importantly, careful studies of the aorta during this same defining period revealed that circumferential lamellar tension ($\sim$2 N/m), and by inference circumferential lamellar stress ($\sim$150 kPa), is similar within the medial layer across multiple mammalian species [7]. This finding, coupled with subsequent observations that aortic material stiffness at mean arterial pressure is also similar ($\sim$500 kPa) across invertebrates and vertebrates [8], strongly suggests the existence of a "mechanical homeostasis"—that is, vascular cells seek to establish and then maintain particular mechanical quantities near target (homeostatic) values. Indeed, findings at subcellular, cellular, tissue, and organ levels suggest that such homeostatic processes exist across many spatial and temporal scales [9].

Two seminal contributions by Fung and his colleagues advanced our ability to quantify arterial wall stress and the associated stiffness, which are important both for assessing the mechanics of the wall and understanding its mechanobiology. First, Fung observed via uniaxial experiments on soft tissues that material stiffness (in this case, a change in the first Piola-Kirchhoff stress with respect to stretch) relates nearly linearly to the stress itself [10]. Importantly, this finding suggests directly that the first Piola-Kirchhoff stress increases nearly exponentially with stretch. Indeed, a similar observation had previously been reported for the overall structural stiffness of the pressurized eye based on its pressure–volume relation [11]. Motivated by these findings, Fung later hypothesized the existence of an exponential stored energy function W that yields an exponential relationship between the second Piola-Kirchhoff stress $\mathbf{S}$ and Green strain $\mathbf{E}$, where $\mathbf{S} = \partial W/\partial \mathbf{E}$. Now known as Fung elasticity, this hyperelastic function can be written as $W = c(\exp(Q) - 1)$, where c is a material parameter and the scalar function Q depends quadratically on $\mathbf{E}$ [12]. An associated metric of material stiffness, in referential form, is thus $\mathbf{C} = \partial \mathbf{S}/\partial \mathbf{E} = \partial^2 W/\partial \mathbf{E}\partial \mathbf{E}$. Notwithstanding the importance of Fung's constitutive hypothesis in quantifying the mechanical behavior of many soft tissues and solving associated initial-boundary value problems, the observation that material stiffness relates linearly to stress implies that it should be challenging to delineate whether mechanobiological responses correlate better with stress or stiffness, consistent with the aforementioned observations that homeostatic values of aortic stress and material stiffness are similar across species [7,8]. Second, Fung showed that the existence of residual stress in arteries dramatically affects the calculated distribution of Cauchy stress $\mathbf{t}$ across the arterial wall [13], which in combination with basal smooth muscle cell tone results in a nearly homogenized transmural distribution [12]. This finding supports the concept that vascular cells seek to establish and then maintain mechanical stress or stiffness near a homeostatic target, regardless of location within the wall. Importantly, it now seems that different homeostatic targets may exist for different cell types that populate different layers of the wall [14], thus reinforcing the concept of a cell-specific mechanical homeostasis that can manifest at the vessel level as well.

The importance of arterial stiffening in human disease was anticipated as early as the turn of the 20th century by Sir W$^{\text{m}}$ Osler, one of four founding fathers of Johns Hopkins medicine, but confirmation had to await a seminal clinical study at Paris, France that revealed that an increased pulse wave velocity (PWV) is an initiator and indicator of diverse cardiovascular, neurovascular, and renovascular disease and thus all-cause mortality [15]. Carotid-to-femoral PWV is now considered to be the gold standard for clinical assessment of arterial stiffness [16], which increases with diabetes, hypertension, natural aging, particular connective tissue disorders, and so forth [17–19]. This metric of stiffness is best measured by dividing the vascular centerline distance between two recording sites by the time that it takes the (foot of the) pressure pulse wave to travel between these sites

[1]Corresponding author.

Manuscript received January 28, 2019; final manuscript received March 25, 2019; published online August 2, 2019. Assoc. Editor: Haichao Han.

("foot-to-foot" PWV). Intuitive understanding of the PWV often comes from the Moens–Korteweg equation, derived in the 1870s and commonly written as $\text{PWV} = \sqrt{Eh/2\rho a}$, where E is an intrinsic (linear) material stiffness, h is the wall thickness, a is the luminal radius, and ρ is the mass density of the fluid. Understood in this way, we see that PWV depends on both the intrinsic material stiffness and the geometry of the wall, hence rendering it an integrated (along the centerline distance) measure of structural, not material, stiffness.

Not surprisingly, there continues to be increasingly greater interest in measuring and understanding arterial stiffness in basic science studies and clinical assessments. Quantifying stiffness helps us to understand critical questions related to, among other issues, fundamental aspects of vascular mechanobiology, effects of a distensible wall on the hemodynamics, disease progression, and even the efficacy of particular clinical treatments. In this paper, we briefly review and contrast different methods for measuring and interpreting arterial stiffness both to emphasize that which has been learned and that which remains unclear. In particular, we emphasize that many different metrics of arterial stiffness reported in the literature have different theoretical underpinnings and thus different meanings. Caution is thus warranted when comparing values of stiffness across studies as well as when interpreting fundamental implications of a particular metric on either the cell biology or the systems physiology.

Approaches

We first review the theoretical basis for some of the experimental methods that are commonly used to infer material properties of the arterial wall and its constituent parts. The presentation is organized by physical scale, not chronological introduction within the field. Regardless of scale, it is critical to delineate concepts of material versus structural stiffness, and similarly, it is essential to note that values of stiffness depend on the type (tensile, compressive, or shear) and magnitude (small or large) of the loading as well as the mechanical state in which the experimental loads are imposed, especially if the sample is otherwise unloaded during testing. Unfortunately, many papers often simply report a value for stiffness without emphasizing the precise definition or experimental conditions, hence obscuring the range of applicability. Here, we attempt to delineate some of these issues.

Atomic Force Microscopy. Invented in the early 1980s at IBM, atomic force microscopy (AFM) uses a laser to detect small deflections of a cantilever probe as it interacts with the surface of a specimen. The atomic force microscope can be used in various modes to assess the topography of a surface or to probe mechanical properties. With regard to the latter, one can perform precise indentation (compression) tests or functionalize the probe to enable tractions (tension) to be applied at the surface. As implied by its name, the most precise atomic force microscopes measure nanoscale forces and motions, thus it is not surprising that AFM has been used extensively in biology, biophysics, and bioengineering, often to assess aspects of cell stiffness, cell-matrix interactions, or local matrix stiffness. With larger probes, one can also assess bulk tissue stiffness. Associated data consist primarily of the applied force (inferred from knowledge of the cantilever properties and deflections) and the imposed motion of the probe, often the depth of penetration into the surface. Quantities such as stress and stiffness can be determined by solving the associated initial-boundary value problem.

Data on indentation force (f) and depth (δ) are often interpreted using a classical 19th century solution by Hertz for the localized indentation of a semi-infinite half-space that exhibits a linearly elastic and isotropic material behavior under small strains and rotations [20]. In this way, one can infer an associated Young's modulus E, a measure of the intrinsic compressive material stiffness for a specialized class of material behaviors. Albeit often not noted, this classical Hertz solution also assumes that the half-space is unloaded prior to the indentation by the probe. Of course, all arteries and their attendant cells are under significant loads in vivo and often are loaded in vitro in cell or organ culture, hence any Young's modulus inferred from the Hertz equation must be viewed cautiously. In particular, it has been shown both analytically [21] and numerically [22] that the indentation force-depth relationship, and thus inferred stiffness, depends strongly on the pre-existing state of stress/strain in the material. Because analytical findings typically provide more intuitive insight than numerical results, note that an exact solution relevant to AFM can be obtained using a theory of small deformations superimposed on large (Appendix A) for the special case of an initially isotropic planar specimen subjected to finite equibiaxial in-plane stretching prior to a superimposed small indentation in the out-of-plane direction [23]. In this case, the indentation force f and (small) depth of penetration δ are related linearly via $f = \alpha\delta$ where the "transverse structural stiffness" α depends nonlinearly on the finite in-plane stretch experienced by the specimen as well as on the intrinsic material stiffness of the material and the geometry of the rigid probe. For example, for a neo-Hookean material behavior defined by a stored energy function $W = \mu(\text{tr}\mathbf{C} - 3)$, where μ is the shear modulus and $\mathbf{C} = \mathbf{F}^{\text{T}}\mathbf{F}$ is the right Cauchy–Green tensor, with $\mathbf{F}$ being the deformation gradient tensor, it can be shown that the transverse stiffness, having units of N/m, can be written as [21]

$$\alpha = 8r_o\mu\frac{(\lambda^9 + \lambda^6 + 3\lambda^3 - 1)}{\lambda^4(\lambda^3 + 1)} \tag{1}$$

where $2r_o$ is the diameter (d_o) of a flat-ended cylindrical probe and λ is the equibiaxial in-plane stretch. A Hertz-type solution can be recovered as $\lambda \to 1$, for which $\alpha \to 16r_o\mu = 4d_oE/3$, with Young's modulus $E(= 6\mu)$ having units of N/m^2. Hence, E can be computed easily given the diameter of the probe and the slope of the force-depth data (f, δ) for an otherwise unloaded specimen. Of course, because of inherent uncertainty in all experimental data, the stiffness parameter(s) should be estimated using least-squares regressions of data via an over-determined system of equations. Moreover, in the case of a nonlinear behavior, the intrinsic material stiffness (e.g., shear modulus μ for a neo-Hookean response) should be inferred from force-depth data over a range of in-plane stretches that are relevant to the biological or physiological regime of interest in order to characterize well the overall material behavior. Noting that adherent cells spread out and develop significant cytoskeletal stress when cultured on any substrate, which is to say that they develop a finite nearly in-plane state of stress or stretch, it has been shown that a small-on-large framework can be used to assess cell stiffness from AFM for more general exponential stored energy functions [24].

Indeed, although a neo-Hookean relation admits a simple analytical solution that allows one to intuit effects of finite in-plane stretches on AFM measured stiffness (Eq. (1)), the Fung exponential model is more appropriate for most soft tissues and even cells. Appendix B summarizes a general Fung model and Appendix C provides results for a small-on-large solution for AFM based on an isotropic Fung exponential model. As expected, the numerical implementation is straightforward. Nevertheless, results from AFM for assessing vascular cell stiffness [25,26] and arterial properties [27–30] typically have been interpreted in terms of a single Young's modulus inferred from the Hertz solution, which tacitly ignores the important nonlinear dependence on in-plane prestretch and the nonlinear (often exponential) material behavior. Hence, the inferred values of stiffness are typically well below in vivo values and could be misleading regarding in vivo mechanobiology.

Although not discussed in detail here, additional methods are also used to assess cell stiffness, including magnetic twisting cytometry (MTC) and optical tweezers [31]. MTC is similar to AFM except that one either affixes onto or embeds within a living cell a ferromagnetic bead that can be cyclically twisted using a

magnetic field. Associated data are often interpreted in terms of the so-called storage (G') and loss (G'') shear moduli, which are basic descriptors of a one-dimensional (1D) linearly viscoelastic behavior over small strains and rotations [32]. For example, MTC was used to show that the stiffness of vascular smooth muscle cells (i.e., elastic storage and dissipative loss moduli) increases in aging [33]. Similar to the Hertz solution, however, this inference of material properties does not explicitly account for the underlying nonlinear material behaviors or the finite deformations that adherent cells experience in vitro when spreading on a surface or to which they are likely exposed in vivo. Again, a small-on-large approach for data analysis could be more appropriate.

Biaxial Biomechanical Testing. Arteries are subjected in vivo to complex multiaxial loads due to blood pressure and flow as well as axial prestresses that develop largely due to somatic growth [12]. Flow-induced shear stresses are important mechanobiologically and can be determined by solving equations that govern the hemodynamics (e.g., Navier–Stokes solutions within the context of fluid–solid interactions), yet they are typically five orders of magnitude smaller (1.5 Pa) than the in-plane intramural stresses (~150 kPa) and thus are neglected in most analyses of the wall stress field. The in-plane circumferential ($t_{\theta\theta}$) and axial (t_{zz}) components of Cauchy stress are tensile, whereas the out-of-plane Cauchy radial (t_{rr}) stress is compressive, on the order of −15 kPa, and typically dictated largely by the traction boundary conditions. For these reasons, biaxial loading has long been preferred for studying the biomechanical properties and function of blood vessels, particularly arteries and veins [34]. Associated pressure-diameter and axial force-length data provide direct insight into the structural stiffness of these vessels. Material stiffness can be inferred from a global equilibrium solution that relates the loads that are measured during standard biaxial tests on excised cylindrical samples to components of the Cauchy stress as [12]

$$P = \int_{r_i}^{r_o} \left(\frac{t_{\theta\theta} - t_{rr}}{r} \right) dr,\ L = \pi \int_{r_i}^{r_o} (2t_{zz} - t_{rr} - t_{\theta\theta}) r dr \qquad (2)$$

where $r \in [r_i, r_o]$, with r_i and r_o being the inner and the outer radius of the sample, respectively, P is the distending pressure, and L is the reduced axial load. If only the mean (i.e., radially averaged, $\langle \ldots \rangle$) values of stress are of interest, then these two integral relations can be replaced with algebraic ones, $\langle t_{\theta\theta} \rangle \equiv \sigma_{\theta\theta} = Pr_i/h$ and $\langle t_{zz} \rangle \equiv \sigma_{zz} = (L + \pi r_i^2 P)/\pi h(2r_i + h)$, where $h = r_o - r_i$ is the wall thickness. Mean values of stress are surprisingly useful because of the aforementioned effect of residual stress in homogenizing the transmural distribution of stress. Regardless, some investigators infer stiffness from plots of stress versus stretch or strain (yielding so-called tangent moduli), but stiffness depends on the full multiaxial deformation and is best computed from an appropriate constitutive relation as noted above for the referential stiffness ($\partial \mathbf{S}/\partial \mathbf{E}$). Given the complex microstructure of the vascular wall, most investigators now prefer the so-called fiber-family constitutive models [35–37] to characterize multiaxial data, though the Fung exponential provides good fits to data in many cases (recall that Appendix B reviews a general orthotropic Fung relation). Best-fit values of material parameters for any appropriate constitutive relation can be determined via nonlinear regression of pressure-diameter and axial force-length data, with data from multiple biaxial protocols typically combined to improve the parameter estimation, again via (nonlinear) least squares regression. In this regard, it is important to note that many studies nevertheless report only pressure-diameter data at a single value of axial stretch and often do not measure the associated axial force. Such data are essentially one-dimensional and not useful for calculating in vivo relevant biaxial stress or stiffness [38].

There are, in addition, a few other issues regarding the in vivo applicability of constitutive relations that are inferred in vitro. First, values of arterial stiffness change with pressure over a cardiac cycle, hence the theory of small deformations superimposed on large has been used to compute "single" values of the spatial material stiffness $\mathbb{C}$ that are often representative over a cardiac cycle and thereby render computations of fluid-solid-interactions more efficient [35]. In component form, we have (see Appendix A)

$$\mathbb{C}_{ijkl} = 2\delta_{ik} F^o_{lA} F^o_{jB} \frac{\partial W}{\partial C_{AB}}\bigg|_{\mathbf{C}^o} + 2\delta_{jk} F^o_{iA} F^o_{lB} \frac{\partial W}{\partial C_{AB}}\bigg|_{\mathbf{C}^o} + 4F^o_{iA} F^o_{jB} F^o_{kP} F^o_{lQ} \frac{\partial^2 W}{\partial C_{AB} \partial C_{PQ}}\bigg|_{\mathbf{C}^o} \qquad (3)$$

where δ_{ij} is the Kronecker delta and a superscript o denotes a deformation quantity that is associated with an original finite deformation about which the small superimposed deformation occurs. For example, the large deformation could be for an artery from a traction-free reference configuration to a finitely distended and extended in vivo configuration near mean arterial pressure about which relatively small motions occur over a cardiac cycle. Second, there is a pressing need to understand better how central arterial stiffness and resistance vessel function interact to affect both local and global hemodynamics and cardiovascular function [19,39]. Third, the effects of perivascular tethering can be as important as the structural stiffness (i.e., material stiffness and geometry) in affecting the hemodynamics though there has not been much quantification of this effect [40,41]. Fourth, constitutive relations that are inferred in vitro are generally established under quasi-static conditions, whereas in vivo loading is pulsatile and hence intrinsically dynamic. Associated differences in strain-rate may influence calculated values of measured stiffness [42,43]. Finally, although well suited for nearly cylindrical samples, standard distension–extension tests are not sufficient for more complex arterial geometries, particularly those manifesting in disease. Fortunately, new methods are emerging that enable local material properties to be inferred using full-field strain measurements and inverse methods for material characterization [44,45].

Although not discussed in detail here, there are also many reports of vascular function and properties based on either uniaxial loading tests (e.g., Ref. [46]) or ring myography (e.g., Ref. [25]). Originally conceived to study isometric contraction, ring tests are performed by placing a short ring-like sample of the vascular wall on two mounting fixtures that are separated by a finite distance. The sample thus stretches primarily in the circumferential direction as the fixtures are separated and the sample deforms from a circular to an oval to a more uniaxial geometry within the central region of measurement. Measurement of the force acting on (passive) or generated by (active) the sample thus allows one to estimate 1D stress-stretch information or to construct dose-response curves while holding a sample at a fixed separation distance (isometric). This approach is particularly valuable for high-throughput comparisons of different drugs or their doses, but the associated contraction of the smooth muscle is under nonphysiological loading [47]. Inference of passive or active stiffness from these ring tests is further compromised by the lack of an exact solution to the full boundary value problem (finite bending and uniaxial extension of an annulus) and the lack of biaxial loading [12,34]. In particular, both the radial and axial stretches reduce below one as circumferential stretch increases with the separation of the mounting fixtures. Axial stretch is typically much greater than unity in vivo and is important to both the mechanics and the mechanobiology [48]. Finally, in-plane biaxial tests can be performed on excised samples (e.g., Ref. [49]) and are generally very informative for they can largely mimic the in vivo state of stress, with the exception of radial compression due to a distending blood pressure. The primary caveat with in-plane biaxial tests is that large specimens can retain some of their natural cylindrical curvature in the unloaded state, thus requiring combined bending and extension to load the sample biaxially. Uniaxial tests performed

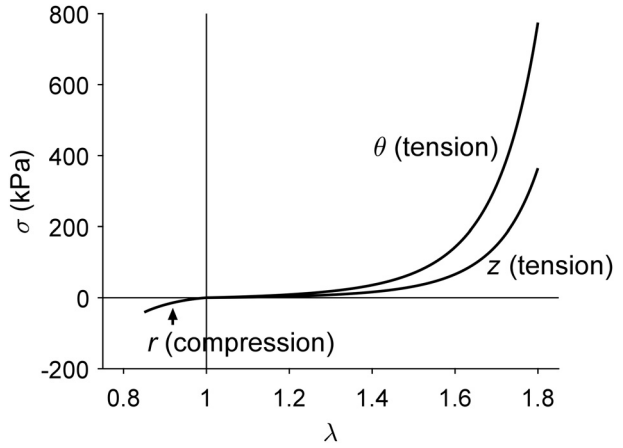

Fig. 1 Intrinsic differences in tensile and compressive Fung-elastic behaviors. Tensile stress-stretch responses are shown for a simulated equibiaxial stretching experiment ($\lambda_\theta = \lambda_z > 1$) in circumferential ($\sigma_{\theta\theta}$ versus λ_θ) and axial (σ_{zz} versus λ_z) directions for mean values of stress (i.e., averaged through the thickness of the sample); note the nonlinear anisotropic behavior. A stress-stretch response is also shown for a simulated uniaxial compression experiment in the radial direction ($\lambda_r < 1$): mean radial Cauchy stress as a function of radial stretch (σ_{rr} versus λ_r). The assumed constitutive behaviors were reported by Chuong and Fung [13,60].

on different samples with different gross orientations can avoid some issues of residual curvature, but associated protocols are limited and cannot explore directly the inherent coupling that is important in dictating the multiaxial mechanical behavior.

Pulse Wave Velocity and Distensibility. Whereas AFM, MTC, biaxial testing, ring myography, and allied methods are employed in vitro on excised samples, which generally enables significant experimental control, clinical studies necessarily require less invasive in vivo methods, measurements, and metrics. As noted earlier, the current clinical gold standard metric of arterial stiffness is the carotid-to-femoral pulse wave velocity, which is a measured quantity that represents a structural response that is integrated over a particular vascular path. There are, in addition, more local metrics of structural stiffness that are used clinically. One such metric is the so-called distensibility

$$D = (d_{\text{sys}}^n - d_{\text{dias}}^n)/d_{\text{dias}}^n(P_{\text{sys}} - P_{\text{dias}}) \tag{4}$$

where d is the luminal diameter, with sys and dias denoting values at systole and diastole, respectively. The parameter $n = 1$ or 2, yielding values of D that differ numerically by approximately a factor of 2. Taking $n = 2$ implies using cross-sectional area rather than diameter, which potentially avoids problems with low spatial imaging resolution. Note further that the Bramwell–Hill form for pulse wave velocity can be written as $\text{PWV} = \sqrt{1/\rho D}$ for $n = 2$, hence localizing the value of PWV. Another local measure of structural stiffness (the pressure–strain or Peterson modulus) can be computed as

$$E_{\text{P}} = (P_{\text{sys}} - P_{\text{dias}})d_{\text{dias}}/(d_{\text{sys}} - d_{\text{dias}}) \tag{5}$$

Clinical findings confirm that local measures such as E_{P} can correlate well with the more global PWV [50], hence suggesting that these metrics are complementary. We end this overview by noting that PWV, D, and E_{P} all intrinsically depend on the operating point (i.e., blood pressure) about which they are measured/calculated [51,52]. In a research setting, such dependence can sometimes be controlled post hoc using regression methods, but this is less feasible in clinical practice. Regression may be especially problematic in studies of hypertension where (a change in) blood pressure may have both direct (through nonlinear mechanics) and indirect (causing arterial remodeling) effects on the measured metric of stiffness, a distinction that cannot be made with regression analyses [53]. This issue motivated considerable research for "pressure-corrected" metrics of stiffness. As should be clear from the preceding text, however, arterial mechanics is highly nonlinear and fully capturing it requires complex constitutive relations with many parameters, with value(s) of stiffness always dependent on the level of stress. Nevertheless, simple metrics have been proposed that, within individual limitations, work surprisingly well [54,55]. Examples include the cardio-ankle vascular indices (CAVI and CAVI_0), which are metrics of global structural stiffness that essentially correct a measured foot-to-foot PWV for its pressure dependence via another metric of local structural stiffness (β and β_0), namely

$$\text{CAVI} = \ln\left(\frac{P_{\text{sys}}}{P_{\text{dias}}}\right)\frac{\text{PWV}^2 \cdot 2\rho}{P_{\text{sys}} - P_{\text{dias}}},$$
$$\text{CAVI}_0 = \frac{\text{PWV}^2 \cdot 2\rho}{P_{\text{dias}}} - \ln\left(\frac{P_{\text{dias}}}{P_{\text{ref}}}\right) \tag{6}$$

$$\beta = \ln\left(\frac{P_{\text{sys}}}{P_{\text{dias}}}\right)\frac{d_{\text{dias}}}{d_{\text{sys}} - d_{\text{dias}}}, \text{ and } \beta_0 = \beta - \ln\left(\frac{P_{\text{dias}}}{P_{\text{ref}}}\right) \tag{7}$$

with P_{ref} being an arbitrary but constant reference value of pressure [56]. These so-called pressure-corrected metrics are motivated by the observation that blood pressure relates approximately exponentially with diameter [55]. CAVI_0 and β_0 represent modifications to the original metrics (CAVI and β) to correspond better with an actual exponential relationship; additionally, CAVI_0 assumes PWV to scale with diastolic instead of mean blood pressure, which seems more in line with experimental observations on the pressure dependency of PWV [51,56].

Of course, PWV can also be estimated using computational methods given much more information: the spatially distributed geometry, material properties, and boundary conditions. Such calculations avoid implicit assumptions inherent in the Moens–Korteweg and related equations and they enable informative parametric studies, as, for example, how vascular taper or distal resistances affect the pulse wave. Unsteady 1D and three-dimensional models have been used to compute PWV [57,58], but again additional intuitive insight can be gleaned from analytical solutions. Toward this end, the theory of small deformations superimposed on large has also been used to obtain analytical results for a simple cylindrical geometry [59]. This solution shows explicitly that both the diastolic distension and the axial prestretch are important contributors to the computed values of PWV; in the limit as the strains become small, this relation recovers the Moens–Korteweg equation. As in the case of the AFM, however, this analysis shows clearly that complexities due to nonlinear material behaviors and finite deformations play important roles in determining the precise value of stiffness that is computed.

Comparisons

Fung and colleagues used nonlinear regression to determine best-fit values of the seven material parameters in an exponential stored energy function W (Eqs. (A1) and (A2) in Appendix B) from both uniaxial (radial compression [60]) and biaxial (pressure-diameter-axial force-stretch [13]) data for a rabbit thoracic artery. Not surprisingly, the parameter values differed for the predominantly compressive versus tensile behaviors. Figure 1 compares these results together; note the anisotropy and strong nonlinearity in the tensile (circumferential and axial) behaviors and the asymmetry between the tensile and compressive behaviors even at modest strains. Results are not shown for greater compressive strains since the original tests used modest levels of compression and the associated analytical solution reveals potential

bifurcations in the equilibrium solutions at higher compressive strains. Importantly, given that the slope of the stress-stretch curves reflects (but does not define) the stretch-dependent spatial material stiffness, note the expected tremendous differences between the low values of material stiffness near the unloaded configuration (low stress) and high values near the in vivo configuration (physiologic stress). Figure 2 shows calculated circumferential behaviors for different degrees of fixed axial stretch from one to the in vivo value (1.691 for this particular rabbit artery). This result reveals the strong biaxial coupling, with circumferential stress and stiffness affected dramatically by the value of axial stretch. The aforementioned ring myography and uniaxial tests disregard such coupling and thus can underestimate the actual stiffness dramatically.

Figure 3 shows calculated results for a simulated AFM indentation test with the material modeled with the same Fung-exponential type of constitutive relation and the indentation performed at different levels of fixed equibiaxial in-plane stretch. Since the analytical small-on-large solution holds for isotropic material behaviors [21], we first estimated new values of the material parameters in the Fung-exponential that yield an isotropic response similar to the mean of the anisotropic response shown in Fig. 1. Again, it can be seen that there is a strongly coupled response between different directions of loading, here out-of-plane versus in-plane. Most published works on arterial wall and vascular cell stiffness disregard this coupling effect and use AFM to test samples, in the absence of a pre-existing in-plane stress, to compute Young's modulus that strictly holds only for small strains. Such a situation is not physiological and again is expected to underestimate the actual in vivo stiffness dramatically.

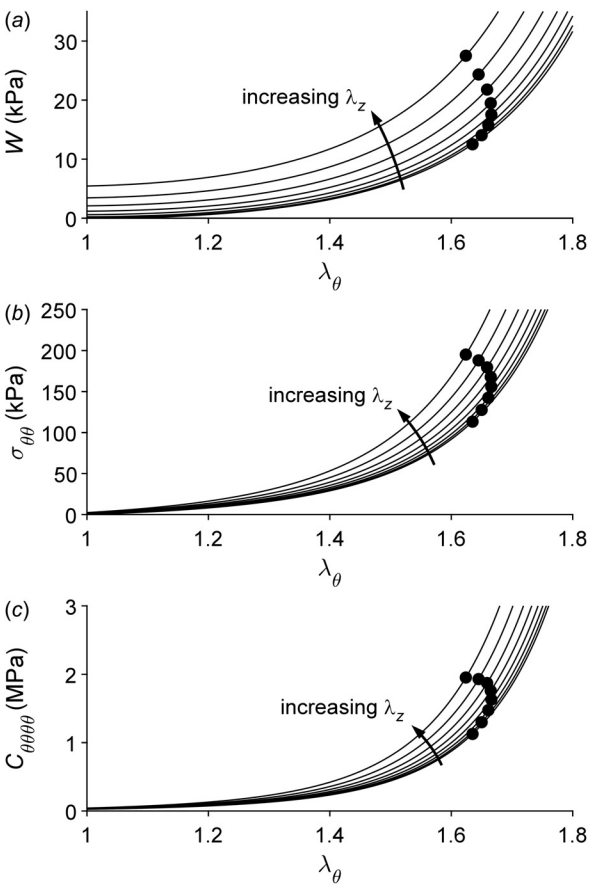

Fig. 2 Circumferential behavior depends strongly on axial stretch. Stored energy *W* (panel *a*), mean circumferential Cauchy stress $\sigma_{\theta\theta}$ (panel *b*), and linearized circumferential material stiffness $\mathbb{C}_{\theta\theta\theta\theta}$ (panel *c*) are shown as a function of circumferential stretch (abscissa) as well as for different values of (constant) axial stretch from 1.0 to 1.7 (8 lines). Black dots correspond to values at a distending pressure of 120 mmHg. Note that mean Cauchy stresses (i.e., integrated through the thickness) are on the order of 150 kPa under physiologic loads, whereas stiffness values are on the order of 1–2 MPa, particularly in a physiologic range of loads.

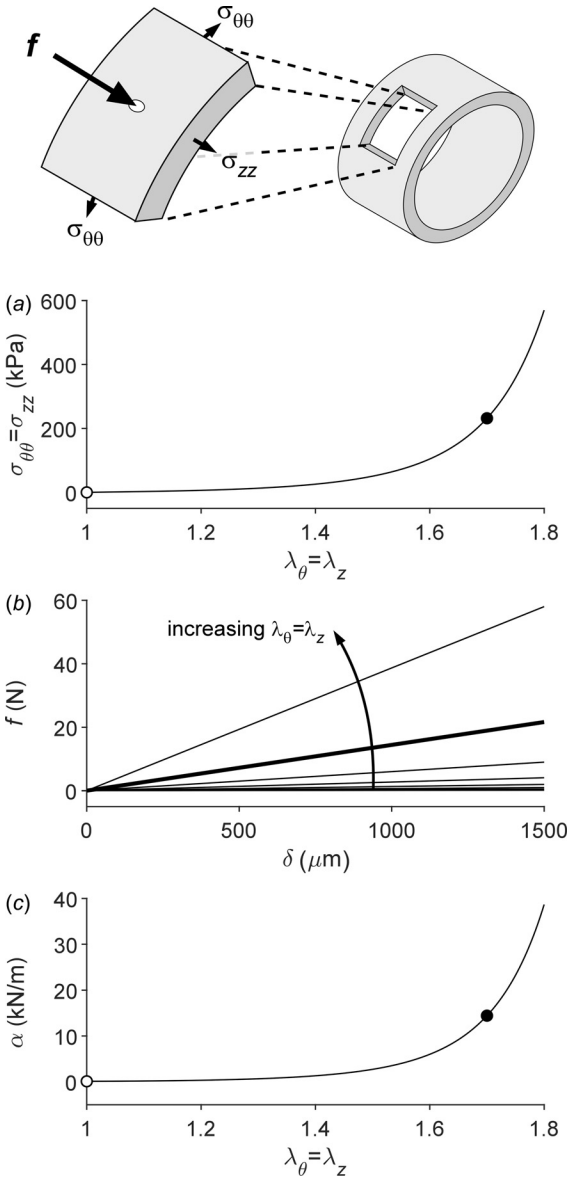

Fig. 3 In-plane prestretch has an important effect on out-of-plane indentation stiffness. The schematic drawing shows a potential arterial wall sample isolated for AFM testing. This planar sample could similarly represent an adherent cell after spreading on a surface. Panel *a* shows the effect of equibiaxial stretching ($\lambda_\theta = \lambda_z \equiv \lambda > 1$) on mean (integrate through the thickness) in-plane Cauchy stress for an assumed isotropic behavior. Panel *b* shows the relationship between indentation force (*f*) and indentation depth (δ) for values of in-plane stretch λ increasing from 1.0 to 1.8 in steps of 0.1. The slope of these lines, effectively the transverse structural stiffness α, is plotted as a function of in-plane equibiaxial stretch λ in panel *c*. Closed dots (panels *a* and *c*) indicate approximate values of the in vivo in-plane stretch ($\lambda_\theta = \lambda_z = 1.70$); open dots indicate the absence of in-plane stretch ($\lambda_\theta = \lambda_z = 1.00$), consistent with many reports in the literature. The thick line in panel *b* similarly corresponds to $\lambda_\theta = \lambda_z = 1.70$. Note the marked effect of in-plane stretching on the out-of-plane (transverse) stiffness as measured, for example, in atomic force microscopy.

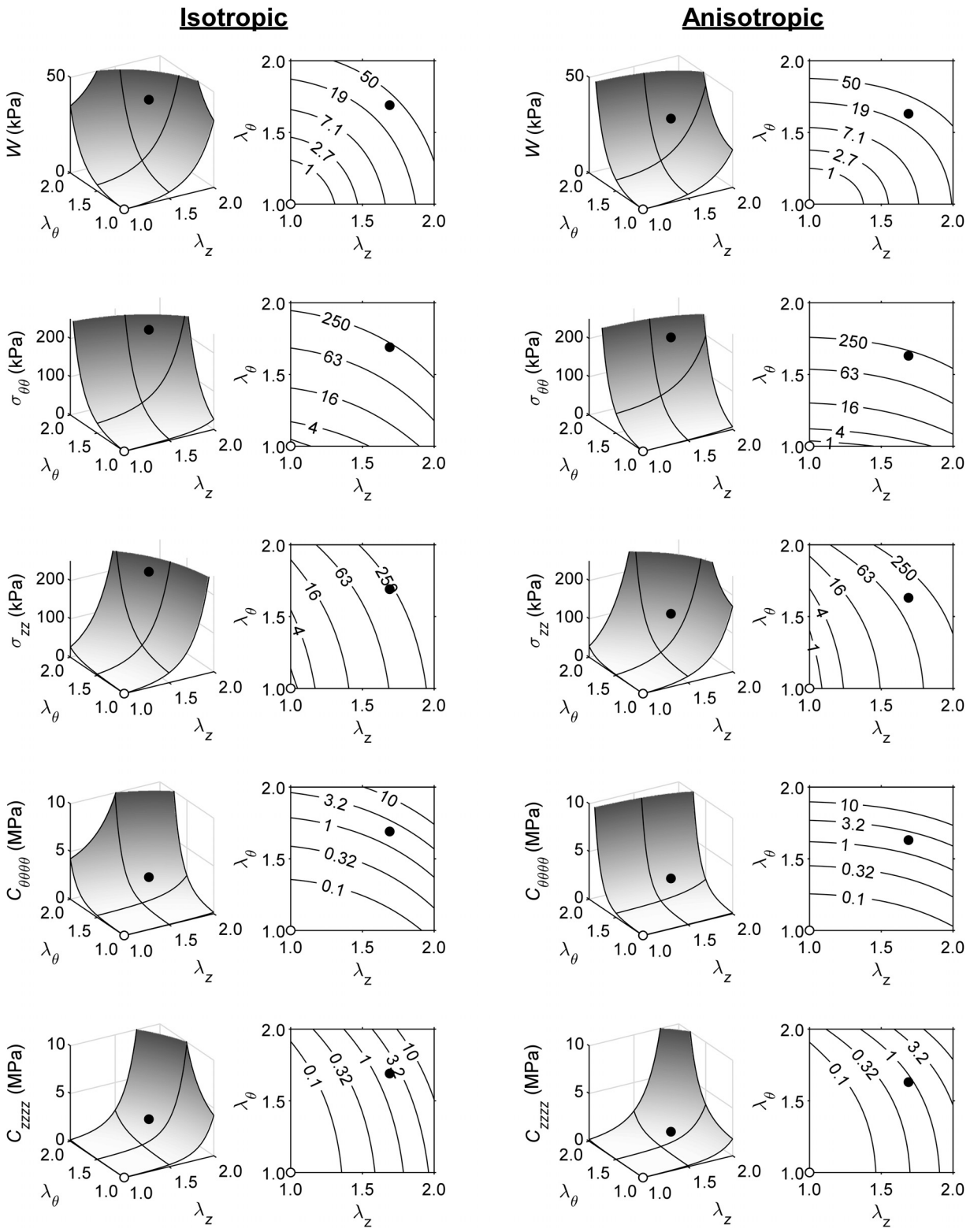

Fig. 4 Linearized spatial material stiffness depends strongly and biaxially on operating point. Panels, from top to bottom, show stored strain energy (W), mean circumferential stress ($\sigma_{\theta\theta}$), mean axial stress (σ_{zz}), circumferential material stiffness ($\mathbb{C}_{\theta\theta\theta\theta}$), and axial material stiffness ($\mathbb{C}_{zzzz}$), all as a function of axial stretch (λ_z) and circumferential stretch (λ_θ). The left two columns correspond to an isotropic Fung relation (Appendix C); the right two columns to an anisotropic Fung relation (Appendix B). Closed dots indicate a possible in vivo operating point at systole ($\lambda_z = 1.69$; $\lambda_\theta = 1.69/1.63$ (isotropic/anisotropic), corresponding to a blood pressure of ~120 mmHg). Open dots indicate an unloaded state ($\lambda_z = \lambda_\theta = 1.00$). Note the large, two orders of magnitude, difference in $\mathbb{C}_{\theta\theta\theta\theta}$ between unloaded ($\mathbb{C}_{\theta\theta\theta\theta} = 0.018/0.024$ MPa (isotropic/anisotropic)) and loaded ($\mathbb{C}_{\theta\theta\theta\theta} = 1.9/2.0$ MPa (isotropic/anisotropic)) states. Black lines on three-dimensional surface plots are projections of the (gray) λ_θ and λ_z gridlines.

To emphasize further both the multiaxial nature of stress and stiffness, and couplings therein, we show three-dimensional plots in Fig. 4 for simple cases of combined circumferential and axial extensions of Fung elastic materials. That is, assuming principal homogeneous deformations and incompressibility, the stored energy function and thus associated wall stress and stiffness depend on the in-plane principal stretches alone. The primary in-plane components of the mean Cauchy stress can thus be thought of conceptually in terms of components of the left stretch tensor $\mathbf{V} = \sqrt{\mathbf{F}\mathbf{F}^{\mathrm{T}}}$, namely $\sigma_{\theta\theta} = \hat{\sigma}_{\theta\theta}(\lambda_\theta, \lambda_z)$ and $\sigma_{zz} = \hat{\sigma}_{zz}(\lambda_\theta, \lambda_z)$. As it can be seen in the figure, for both isotropic (left columns; cf. Fig. 3) and anisotropic (right columns; cf. Figs. 1 and 2) behaviors, circumferential and axial deformations contribute similarly to the overall elastic energy storage and thus stress and material stiffness, here in a spatial rather than referential description since spatial quantities (defined relative to the current configuration) are most relevant in vivo.

Discussion

It is now widely accepted that both cell- and matrix-level stiffness are fundamental to mechanobiological responses within the vasculature, including modulation of cell phenotype. Similarly, it is widely accepted that tissue-level stiffness is fundamental to the hemodynamics, particularly propagation of the arterial pressure wave that dictates many aspects of end organ health or disease. There is, therefore, an appropriately growing literature on arterial stiffness. Yet, the many different reported metrics have different meanings because of different types of loads that are imposed relative to different biomechanical states. We summarize in Table 1 some of these methods and metrics and, for purposes of illustration, we list in Table 2 some values of stiffness resulting from these different methods. As it can be seen, reported values of stiffness (some compressive, some shear, most tensile) differ by orders of magnitude, as should be expected for highly nonlinear material behaviors when assessed relative to different configurations, ranging from otherwise unloaded to in vivo relevant. Assuming that the associated calculations were performed correctly, each of these different values of stiffness should be viewed as reliable. The key question, which we do not attempt to answer here, is therefore: How can we extract from these disparate metrics, having different meanings, a unified understanding of vascular cell mechanobiology and biomechanics and their roles in dictating vascular health or disease progression? We submit that focused effort should be directed toward answering this question, for without such our ability to use basic science findings to inform clinical decisions will remain largely wanting since understanding will remain largely fragmented and incomplete.

In some ways, we have emphasized the obvious—the value of stiffness depends on its definition (material versus structural), the configuration to which it refers (referential-unloaded, versus spatial-current), and the conditions under which it is evaluated (compression versus tension versus shear in an otherwise unloaded state or not). Yet, we are not aware of a prior consistent discussion of methods used in vascular mechanics across scales from atomic force microscopy to biaxial tests on cylindrical segments to in vivo measurements. As we have noted, a number of metrics reported in the literature are based on solutions from classical elasticity because of the associated simplicity, not the theoretical relevance. Strictly speaking, therefore, most of these results are applicable only for linearly elastic isotropic responses under small strains and rotations when measured about an unloaded state—conditions not applicable to mechanobiologically, physiologically, or clinically relevant situations. Although we noted two analytical examples wherein a material stiffness applicable to a nonlinear behavior can be compared directly in the limit to a small strain Young's modulus [21,59], it is generally problematic and uninformative to compare findings based on Hertz, Moens–Korteweg, or similar equations with those based on nonlinear constitutive relations or appropriate linearizations thereof, including the theory of small deformations superimposed on large. Yet, values of Young's modulus continue to be reported and, in some cases, results are similarly presented based on concepts from linearized viscoelasticity, including storage and loss moduli. Of course, one could argue that such results can be insightful when one consistently compares values across studies using the same methods and metrics whether they strictly hold theoretically or not in configurations relevant to in vivo conditions or not. For example, a compressive Young's modulus inferred from AFM has been reported by multiple groups to increase for isolated smooth muscle cells in aging and hypertension relative to that in normalcy [25,69], hence these data are trying to tell us something—the question is, What? That is, although results may be reproducible and reliable, the key question should focus on their possible relevance in vivo. Similar methods have been used to show that the nuclear protein lamin-A scales with tissue stiffness [70], with tissues ranging from compliant (adipose or liver) to stiff (ligaments and bones). Again, the results are reproducible, reliable, and provocative, though not evaluated at in vivo values of stiffness. How such results should be interpreted or compared to values that are relevant to the in vivo condition remains an open question.

We submit that in vivo relevant conditions and metrics should be used when possible. Toward this end, the theory of small deformations superimposed on large deformations [71] can serve as a theoretically appropriate method to compute linearized values of

Table 1 Arterial stiffness—measurement modalities, metrics, and characteristics

Modality	Application	Configuration for stiffness measurement	Vascular axes of stiffness measurement	Mode of stiffness measurement	Loading rate	Typical output metric (s)
Atomic force microscopy	In vitro	Unloaded[1]	Radial or axial	Compressive	Quasi-static	*E* (M)
Wire myography	In vitro	Uniaxially loaded	Circumferential	Tensile	Quasi-static[2a]	*E* (M), *C* (S)
Pressure myography	In vitro	Uniaxially or biaxially loaded	Circumferential and axial	Tensile	Quasi-static[2b]	*E* (M), W (M), *C* (S)
Biomechanical biaxial testing	In vitro	Biaxially loaded	Circumferential and axial	Tensile	Quasi-static	*W* (M), C (S)
Surface transit time PWV	In vivo	Loaded	—	Tensile	Dynamic	PWV (S)
Magnetic Resonance Imaging	In vivo	Loaded	Circumferential	Tensile	Dynamic	*C* (S), *D* (S), PWV (S)[3,4]
Ultrasound echotracking	In vivo	Loaded	Circumferential	Tensile	Dynamic	*E* (M), *C* (S),*D* (S), PWV (S)[3]

C, compliance coefficient; *D*, distensibility; *E*, Young's modulus; *W*, strain energy; PWV, pulse wave velocity. M, material stiffness metric; S, structural stiffness metric.
[1]Typically unloaded, but has been performed on tissue maintained in a biaxially loaded state [61];
[2]typically quasi-static, but has been performed under dynamic loading ([a][62], [b][63]);
[3]calculated using the Bramwell–Hill relationship;
[4]measured by estimating transit time.

Table 2 Values of aortic stiffness (mouse) depend strongly on methodology

Vessel/mouse	Modality	Definition/state	Value, units, age	Reference
Thoracic aorta, C57BL/6J (age 2–18 months)	AFM	In Vitro, unloaded, cut open, radially indented from luminal side (endothelium intact)/compressive	$E = 3.1$ kPa (2 months) $E = 3.6$ kPa (6 months) $E = 16.9$ kPa (12 months) $E = 21.8$ kPa (18 months)	[29]
Suprarenal abdominal aorta, C57/Sv129 (age 10–13 months)	AFM	In Vitro, unloaded or pressurized to 100 mmHg and elongated to In Vivo axial stretch, ring, axially indented/compressive	$E = 18.7$ kPa (unloaded) $E = 12.3$–76.4 kPa (loaded; bimodal distribution)	[61]
Aorta, C57BL/6J (age 11 months)	AFM	In Vitro, unloaded, cut open, radially indented from luminal side (endothelium removed)/compressive	$E = 24$ kPa	[28]
Ascending thoracic aorta, C57BL/6J (age 0.5–3.5 months)	AFM	In Vitro, unloaded, cut open, radially indented from luminal side (endothelium intact)/compressive	$E = 2.8$–12.7 kPa (0.5 months)[1] $E = 5.0$–38.8 kPa (2 months)[1] $E = 4.4$-36.7 kPa (3.5 months)[1]	[30]
Ascending thoracic aorta, C57BL/6J (age 15.2±0.1 weeks)	Biaxial testing	In Vitro, loaded, intact, pressurized to 128 mmHg, elongated to In Vivo axial stretch/tensile	$\mathbb{C}_{\theta\theta\theta\theta} = 2.76$ MPa $\mathbb{C}_{zzzz} = 2.26$ MPa	[64]
Suprarenal abdominal aorta, C57BL/6J (age 5–6 months)	Biaxial testing	In Vitro, loaded, intact, pressurized to 100 mmHg, elongated to In Vivo axial stretch/tensile	$\partial S_{\theta\theta}/\partial E_{\theta\theta} = 1.33$ MPa $\partial S_{zz}/\partial E_{zz} = 0.082$ MPa	[65]
Carotid-to-femoral arterial bed, C57BL/6J (age 5.6±0.2 months)	Applanation tonometry	In Vivo, 4–5% sevoflurane or 75 mg/kg sodium pentobarbital anesthesia, noninvasive/PWV	PWV = 3.96 m/s (sevoflurane)[2] PWV = 2.89 m/s (sodium pentobarbital)[2]	[66]
Abdominal aorta, C57BL/6 (age 3–4 months)	Ultrasound echotracking	In Vivo, 125 mg/kg tribromoethanol anesthesia, noninvasive/PWV	PWV = 2.70 m/s[3]	[67]
Aorta (regionally dependent), C57BL/6J (age 3 months)	Ultrasound echotracking/pressure catheter	In Vivo, 1.5% Isoflurane anesthesia, noninvasive (ultrasound), invasive (catheter)/PWV	PWV = 5.2 m/s[4] PWV = 3.0 m/s[5] PWV = 3.5 m/s[6]	[68]

E, Young's modulus.
[1]Computationally separated, numbers denote intimal/medial moduli. AFM, atomic force microscopy; PWV, pulse wave velocity; $\mathbb{C}_{\theta\theta\theta\theta}$ and $\mathbb{C}_{zzzz}$, linearized circumferential and axial spatial material stiffness obtained using the theory of small-on-large. $\partial S_{\theta\theta}/\partial E_{\theta\theta}$ and $\partial S_{zz}/\partial E_{zz}$, referential material stiffness defined as the derivative of second Piola-Kirchhoff stress with respect to Green strain;
[2]carotid-to-femoral transit-time PWV;
[3]PWV in the window of an ultrasound probe;
[4]aortic arch-to-femoral bifurcation transit-time PWV (ultrasound);
[5]abdominal transit-time PWV (blood pressure catheter, 2 cm path length);
[6]distensibility-based local abdominal PWV obtained from Bramwell–Hill equation. In studies where interventions were performed, control groups are displayed here.

stiffness while accounting for underlying nonlinear material behaviors and in vivo relevant finite deformations, with applicability including interpretations of AFM data [21], defining biaxial material stiffness in intact excised vessels for simulations of hemodynamics [35], and computing PWV either analytically [59] or numerically [58]. With regard to the need to measure and report metrics that are relevant to the in vivo conditions, it would be prudent to remember the words of Y. C. Fung written ∼50 years ago. First, "The main difficulty [problem] lies in the customary use of infinitesimal theory of elasticity to the media which normally exhibit finite deformations" [10] and "the greatest need lies in the direction of collecting data in multiaxial loading conditions and formulating a [constitutive] theory for the general rheological behavior of living tissues…" [72].

In conclusion, it is critical to quantify arterial stiffness—material and structural—because deviations from normal values associate with both the phenotypic modulation of vascular cells and the clinical severity of disease or disease risk. That said, there is also a fundamental conceptual issue that must be considered carefully as we seek to advance our understanding of the underlying mechanobiology. Although vascular cells clearly attempt to establish and then maintain certain mechanical quantities near homeostatic values [9,73], the continuum quantities of stress and strain, and metrics such as material stiffness that are derived from them, are actually mathematical concepts, not physical realities [74]. Hence, even though it appears that mean wall stress and stiffness are normally regulated near homeostatic targets across mammalian species [7,8,75], we should not expect a cell to necessarily respond to a stress (i.e., a linear transformation, or tensor, that transforms an outward unit vector into a traction vector at a point). Rather, it is more likely that forces acting at the molecular level change the conformation of important biomolecules and thereby stimulate cell signaling and downstream gene products. There is, therefore, a pressing need to understand better the micromechanics of mechanosensing by cells and the associated mechanoregulation of matrix [76] and to associate such phenomena with convenient continuum metrics such as stress and stiffness. Nevertheless, until, and possibly after, such multiscale understanding is achieved, direct correlations of mechanobiological and (patho)-physiological responses with wall stress and stiffness should continue to be identified. Toward this end, an increased use of concepts of nondimensionalization and allometric scaling [77] should also become a priority. There is, therefore, a need for continued development of new concepts and techniques in vascular mechanics and mechanobiology and we conclude with words of Fung in his foreword to the inaugural issue of the journal *Biomechanics and Modeling in Mechanobiology* in 2002 [78]—"let us enjoy the work."

Acknowledgment

JDH also gratefully acknowledges the Y.C. Fung Young Investigator Award from ASME that he received in 1990.

Funding Data

- US NIH (Funder ID: 10.13039/100000002; Grant Nos. R01 HL105297, P01 HL134605).
- Netherlands Organization for Scientific Research (NWO) (Funder ID: 10.13039/501100003246; Rubicon Grant 452172006).

Appendix A: Small on Large

The polymath A. Cauchy knew equations of nonlinear elasticity in the 1820s, but analytical solutions to this class of problems had to await the semi-inverse approach of R. Rivlin in the late 1940s. Because of the inherent complexities, analytical solutions to problems in nonlinear elasticity were yet possible for only a relatively small class of motions [79] and many employed the advances in finite element methods that soon arrived [80]. It is often difficult to develop intuition from numerical solutions of highly nonlinear problems, however, thus the concept of "small deformations superimposed on large deformations" became useful in extending the range of possible analytical solutions. As noted herein, small-on-large solutions have been found useful in interpreting experimental results associated with atomic force microscopy [21], quantifying mechanical properties from biaxial tests on excised arteries [35], and relating the structural stiffness that can be inferred in vivo from measurements of pulse wave velocity to the material stiffness inferred from in vitro tests [59]. It seems appropriate, therefore, to briefly outline steps of this approach; the interested reader is referred elsewhere for more details [71].

Briefly, let the location of a material particle in an original configuration be denoted by $\boldsymbol{X}$ and in a finitely deformed configuration by $\boldsymbol{x}$. In addition, let the location of this particle in a configuration that is close to the finitely deformed one be denoted by $\boldsymbol{y}$. The total deformation gradient is thus $\mathbf{F} = (\partial \boldsymbol{y}/\partial \boldsymbol{x})(\partial \boldsymbol{x}/\partial \boldsymbol{X})$, which can be written as $\mathbf{F} = \mathbf{F}_s\mathbf{F}_o$, where subscript o denotes the original finite deformation and subscript s denotes the superimposed small deformation. It proves convenient to write $\boldsymbol{y} = \boldsymbol{x} + \boldsymbol{u}$, where $\boldsymbol{u}$ is a small displacement vector. Hence, $\mathbf{F}_s = \partial \boldsymbol{x}/\partial \boldsymbol{x} + \partial \boldsymbol{u}/\partial \boldsymbol{x}$ which we write as $\mathbf{F}_s = \mathbf{I} + \mathbf{h}$, where $\mathbf{h}$ is a displacement gradient with $|\mathbf{h}| = \sqrt{tr(\mathbf{h}\mathbf{h}^{\mathrm{T}})} \ll 1$. The right Cauchy–Green tensor can then be written as $\mathbf{C} = \mathbf{F}^{\mathrm{T}}\mathbf{F} = [(\mathbf{I}+\mathbf{h})\mathbf{F}_o]^T[(\mathbf{I}+\mathbf{h})\mathbf{F}_o] = \mathbf{F}_o^T\mathbf{F}_o + \mathbf{F}_o^T\mathbf{h}^T\mathbf{F}_o + \mathbf{F}_o^T\mathbf{h}\mathbf{F}_o + \mathbf{F}_o^T\mathbf{h}^T\mathbf{h}\mathbf{F}_o \cong \mathbf{C}_o + \mathbf{F}_o^T(\mathbf{h}^T + \mathbf{h})\mathbf{F}_o = \mathbf{C}_o + \mathbf{F}_o^T(2\boldsymbol{\varepsilon})\mathbf{F}_o$ if we neglect terms that are higher order in the (small) displacement gradient and we recognize the small strain tensor $\boldsymbol{\varepsilon} = (\mathbf{h} + \mathbf{h}^T)/2$. Hence, the right Cauchy–Green tensor in the final configuration simply equals that in an intermediate (finitely deformed) configuration, denoted by subscript o, plus a part that is linear in the small displacement gradient.

Just as the total deformation gradient $\mathbf{F} = (\mathbf{I}+\mathbf{h})\mathbf{F}_o = \mathbf{F}_o + \mathbf{h}\mathbf{F}_o$ consists of a contribution that is due to a finite deformation to an intermediate configuration plus an addition, one can also assume that the total second Piola-Kirchhoff stress can be computed as $\mathbf{S} = \mathbf{S}_o + \mathbf{S}^*$, where the first contribution is associated with the original finite deformation and the second with a superimposed small deformation, namely $\mathbf{S}^* \cong (\partial \mathbf{S}/\partial \mathbf{C})|_o : \mathbf{C}^*$ with $\mathbf{S} = \partial W/\partial \mathbf{C}|_o$ and $\mathbf{C}^* = \mathbf{C} - \mathbf{C}_o = \mathbf{F}_o^{\mathrm{T}}(2\boldsymbol{\varepsilon})\mathbf{F}_o$ from above. Importantly, it can be shown that we can write the total Cauchy stress $\mathbf{t}$, for an incompressible response and to order $|\mathbf{h}|$, as [35] $\mathbf{t} = \mathbf{t}_o + \mathbf{h}\hat{\mathbf{t}}_o + \hat{\mathbf{t}}_o\mathbf{h}^{\mathrm{T}} - p^*\mathbf{I} + \mathbf{F}_o\hat{\mathbf{S}}^*\mathbf{F}_o^{\mathrm{T}}$, where $\hat{\mathbf{t}}_o$ is the extra (i.e., deformation-dependent) part of the Cauchy stress in the finitely deformed intermediate configuration and p^* is a Lagrange multiplier that enforces isochoric motions during the small superimposed deformation. Finally, using the result above for the second Piola-Kirchhoff stress in terms of the stored energy function W, and recognizing that a small displacement gradient can be written in terms of the infinitesimal strain and rotation (i.e., $\mathbf{h} = (\mathbf{h} + \mathbf{h}^T)/2 + (\mathbf{h} - \mathbf{h}^T)/2$, or, $\mathbf{h} = \boldsymbol{\varepsilon} + \boldsymbol{\Omega}$), we arrive at our final result: $\mathbf{t} + p^*\mathbf{I} = \mathbf{t}_o + \mathbb{C}\boldsymbol{\varepsilon} + \mathbb{D}\boldsymbol{\Omega}$, where the spatial material stiffness (fourth order) tensor $\mathbb{C}$ can be written for an artery as given in component form in the third equation in the main text. Noting that the infinitesimal rotation tensor $\boldsymbol{\Omega}$ vanishes with assumed principal deformations, this derivation reveals clearly that the spatial material stiffness associated with a superimposed small deformation depends directly and strongly on the prestress (or prestretch) and the nonlinear properties represented by W, which are amplified nonlinearly by the initial finite deformation when evaluated in the current (spatial) configuration [35].

Appendix B: Fung Elasticity

The illustrative solutions in Figs. 1–4 were obtained using the same Fung exponential strain energy function to facilitate comparisons across methods. This function is defined by [12]

$$W = \frac{1}{2}c(e^Q - 1) \tag{A1}$$

where, in terms of principal Green strains,

$$Q = b_1E_{\Theta\Theta}^2 + b_2E_{ZZ}^2 + b_3E_{RR}^2 + 2b_4E_{\Theta\Theta}E_{ZZ} + 2b_5E_{ZZ}E_{RR} + 2b_6E_{RR}E_{\Theta\Theta} \tag{A2}$$

with c and b_j $(j = 1, 2, \ldots, 6)$ being material parameters that need to be determined from nonlinear regressions of data. For principal deformations, as of interest herein, the Green strains $E_{ii} = (\lambda_i^2 - 1)/2$ for (no sum on) $i = \{\Theta, Z, R\}$.

Uniaxial Compression. Uniaxial radial compression testing comparable to that reported by Chuong and Fung [60] was simulated by prescribing radial stretches λ_r from 1 to 0.85 (Fig. 1, negative abscissa). Incompressibility was assumed, and circumferential and axial directions were assumed to be traction-free consistent with the reported experiment, though it would have been better, albeit difficult, to have induced a finite in-plane deformation prior to the radial compression. Nonetheless, given the assumption of a homogeneous deformation, the in-plane Cauchy stresses in the actual experiment were $t_{\theta\theta} = t_{zz} = 0$. Constitutively, Cauchy stress was calculated from W as

$$t_{ii} = -p + \lambda_i^2\frac{\partial W}{\partial E_{ii}}, \text{with no sum on } i = \{\theta, z, r \text{ or } \Theta, Z, R\} \tag{A3}$$

with p being a Lagrange multiplier enforcing incompressibility. From the traction-free conditions and homogeneous state of deformation, the Lagrange multiplier p for compression tests (p_{comp}) can be determined from Eq. (A3) using either

$$p_{\mathrm{comp}} = \lambda_\theta^2\frac{\partial W}{\partial E_{\Theta\Theta}} \quad \text{or} \quad p_{\mathrm{comp}} = \lambda_z^2\frac{\partial W}{\partial E_{ZZ}} \tag{A4}$$

after which either λ_θ was determined as $\lambda_\theta = 1/(\lambda_z\lambda_r)$ with λ_z determined iteratively to satisfy $t_{zz} = 0$ or vice versa for the axial stretch. Numerical simulations revealed equivalent outcomes using these two constraints.

Simulations of the compression experiment were then performed using reported values of the constitutive parameters for a rabbit thoracic artery (sample 11, incompressible case) given in Ref. [60]: $c = 43.12\,\mathrm{kPa}$, $b_1 = 0.8230$, $b_2 = 0.9125$, $b_3 = 1 \times 10^{-7}$, $b_4 = 1.1237$, $b_5 = 0.4125$, and $b_6 = 0.3768$.

Biaxial Stretching. Equibiaxial in-plane stretch testing similar to that performed by Vande Geest et al. [49] was simulated by prescribing $\lambda_\theta = \lambda_z$ from 1.0 to 1.8 (Fig. 1, positive abscissa),

with $\lambda_r = 1/(\lambda_\theta \lambda_z)$. Cauchy stress was then obtained using Eq. (A3), with p (p_{tension}) determined from $t_{rr} = 0$, because of the traction-free condition on the top and bottom surfaces and the assumed homogeneous deformation, as

$$p_{\text{tension}} = \lambda_r^2 \frac{\partial W}{\partial E_{RR}} \tag{A5}$$

Simulations of tensile loading were performed using values of the constitutive parameters, again for a rabbit thoracic artery [13]: $c = 22.40\,\text{kPa}, b_1 = 1.0672, \quad b_2 = 0.4775, \quad b_3 = 0.0499, b_4 = 0.0903, b_5 = 0.0585$, and $b_6 = 0.0042$. Note the differences between the values for compression and tension despite the same functional form of W and the same sample tested by the same investigators.

Additional in-plane biaxial tension experiments (tension in θ and z directions), with $\lambda_\theta \neq \lambda_z$ but $t_{rr} = 0$, were simulated with the same tensile constitutive parameters (c, b_1–b_6) that were used in the prior section. Such loading simulates possible in-plane biaxial testing [49] but also mimics mean values of stress in possible distension–extension tests [38]. Indeed, corresponding in vivo loading states were determined by simulating pressure-diameter testing as follows. Unloaded inner and outer radii were $R_\text{i} = l_\text{i}/(2\pi)$ and $R_\text{o} = l_\text{o}/(2\pi)$, with $l_\text{i} = 8.75\,\text{mm}$ and $l_\text{o} = 12.5\,\text{mm}$ the inner and outer unloaded circumferences given in Ref. [13], with unloaded thickness $H = R_\text{o} - R_\text{i}$. Loaded inner radius r_i was varied iteratively and loaded outer radius r_o was computed as

$$r_\text{o} = \sqrt{r_\text{i}^2 + \frac{R_\text{o}^2 - R_\text{i}^2}{\lambda_z}} \tag{A6}$$

with loaded thickness $h = r_\text{o} - r_\text{i}$. The mean circumferential stretch λ_θ is then

$$\lambda_\theta = \frac{r_\text{i} + \frac{h}{2}}{R_\text{i} + \frac{H}{2}} \tag{A7}$$

Prescribing axial stretch λ_z allows the radial stretch λ_r to be determined from incompressibility ($\lambda_r = 1/(\lambda_\theta \lambda_z)$). Components of Cauchy stress again follow from Eq. (A3) and p from Eq. (A5). Luminal distending pressure P is now obtained from the mean value of Cauchy stress and geometry as

$$P = \frac{h \cdot \sigma_{\theta\theta}}{r_\text{i}} \tag{A8}$$

Increasing values of r_i thus yield desired increases in pressure (e.g., up to 120 mmHg).

Appendix C: Simulations of Atomic Force Microscopy for Fung Elasticity

The effect of in-plane prestretch on out-of-plane indentation testing, as in AFM, was simulated using the solution in Ref. [21]. For these derivations to hold, the in-plane stretch must be equibiaxial and the material must be isotropic. For consistency with our other simulations (Appendix B), we again used a Fung exponential strain energy function, though one that is parameterized isotropically, namely

$$b_1 = b_2 = b_3 \;\text{ and }\; b_4 = b_5 = b_6 \tag{A9}$$

To obtain parameter values that model tension similar to the mean anisotropic response shown in Fig. 1, we simulated equibiaxial testing of an isotropic Fung elastic material (described by unique parameters c, b_1, and b_4), and fitted these three parameters to the mean of the anisotropic case. Specifically, we calculated the homogeneous (mean) equibiaxial Cauchy stresses $\sigma_{\theta\theta}^{\text{iso}} = \sigma_{zz}^{\text{iso}}$, and minimized

$$e\left(c, b_1, b_4\right) = \sum_{k=1}^{N} \left[\left(\sigma_{\theta\theta}^{\text{aniso}} - \sigma_{\theta\theta}^{\text{iso}}(c, b_1, b_4)\right)_k^2 + \left(\sigma_{zz}^{\text{aniso}} - \sigma_{zz}^{\text{iso}}(c, b_1, b_4)\right)_k^2\right] \tag{A10}$$

with $\sigma_{\theta\theta}^{\text{aniso}} \neq \sigma_{zz}^{\text{aniso}}$ being the anisotropic Cauchy stresses shown in Fig. 1 (positive abscissa), with k a data point index and N the total number of data points (i.e., equilibrium configurations assessed during testing). This procedure yielded $c = 26.97\,\text{kPa}$, $b_1 = b_2 = b_3 = 0.6685$, and $b_4 = b_5 = b_6 = 0.2823$, here for a "virtual" rabbit thoracic artery.

To use the formulation in Ref. [21], we reformulated the isotropic form of W in terms of invariants of the Green strain tensor $\mathbf{E}$, namely $I_\mathbf{E}$ and $II_\mathbf{E}$, and then wrote W in terms of invariants of the right Cauchy–Green tensor $\mathbf{C} = 2\mathbf{E} + \mathbf{I}$. Toward this end, we used the full formulation for Q [12] where

$$\begin{aligned} Q = {} & b_1 E_{\Theta\Theta}^2 + b_2 E_{ZZ}^2 + b_3 E_{RR}^2 + 2b_4 E_{\Theta\Theta} E_{ZZ} + 2b_5 E_{ZZ} E_{RR} \\ & + 2b_6 E_{RR} E_{\Theta\Theta} + b_7 \left(E_{\Theta Z}^2 + E_{Z\Theta}^2\right) + b_8 \left(E_{ZR}^2 + E_{RZ}^2\right) \\ & + b_9 \left(E_{R\Theta}^2 + E_{\Theta R}^2\right) \end{aligned} \tag{A11}$$

which for isotropy (Eq. (A9) and $b_7 = b_8 = b_9$), with $b_7 = b_1 - b_4$, can be written as

$$\begin{aligned} Q = {} & a(E_{\Theta\Theta} + E_{ZZ} + E_{RR})^2 + b(E_{\Theta\Theta} E_{ZZ} + E_{ZZ} E_{RR} \\ & + E_{RR} E_{\Theta\Theta} - E_{R\Theta} E_{\Theta R} - E_{\Theta Z} E_{Z\Theta} - E_{ZR} E_{RZ}) \end{aligned} \tag{A12}$$

or more compactly

$$Q = a I_\mathbf{E}^2 + b II_\mathbf{E} \tag{A13}$$

with

$$\begin{aligned} I_\mathbf{E} &= E_{\Theta\Theta} + E_{ZZ} + E_{RR} \\ II_\mathbf{E} &= E_{\Theta\Theta} E_{ZZ} + E_{ZZ} E_{RR} + E_{RR} E_{\Theta\Theta} - E_{R\Theta} E_{\Theta R} \\ & \quad - E_{\Theta Z} E_{Z\Theta} - E_{ZR} E_{RZ} \end{aligned} \tag{A14}$$

because $\mathbf{E}$ is a symmetric tensor. Note, too, that the two (exponential) material parameters for isotropy are $\mathrm{a} = b_1$ and $\mathrm{b} = 2(b_4 - b_1) = -2b_7$ (with $b_1 > b_4$). Next, recognize that the right Cauchy–Green tensor $\mathbf{C}$, with invariants $I_\mathbf{C}$ and $II_\mathbf{C}$

$$I_\mathbf{C} = 2(E_{\Theta\Theta} + E_{ZZ} + E_{RR}) + 3 = 2I_\mathbf{E} + 3 \tag{A15}$$

and

$$\begin{aligned} II_\mathbf{C} = {} & 4(E_{\Theta\Theta} E_{ZZ} + E_{ZZ} E_{RR} + E_{RR} E_{\Theta\Theta}) - 4\left(E_{\Theta Z}^2 + E_{ZR}^2 + E_{\Theta R}^2\right) \\ & + 4(E_{\Theta\Theta} + E_{ZZ} + E_{RR}) + 3 = 4I_\mathbf{E} + 4II_\mathbf{E} + 3 \end{aligned} \tag{A16}$$

Re-arranging Eqs. (A15) and (A16) and inserting into Eq. (A13) yields

$$Q = \frac{1}{4} a I_\mathbf{C}^2 - \left(\frac{3}{2}a + \frac{1}{2}b\right) I_\mathbf{C} + \frac{1}{4}\mathrm{b} II_\mathbf{C} + \frac{9}{4}a + \frac{3}{4}b \tag{A17}$$

Given $W(Q)$ written in this form, the equations in Ref. [21], written as functions of $\partial W/\partial I_C$ and $\partial W/\partial II_C$, can be used directly to simulate AFM indentations for an isotropic Fung elastic material, similar to the calculation discussed in the text for the simpler neo-Hookean material.

References

[1] Roy, C. S., 1881, "The Elastic Properties of the Arterial Wall," J. Physiol., **3**(2), pp. 125–159.

[2] Thoma, R., 1893, *Untersuchungen Über Die Histogenese Und Histomechanik Des Gefäßsystems*, Enke, Stuttgart, Germany.
[3] Rosen, L. A., Hollis, T. M., and Sharma, M. G., 1974, "Alterations in Bovine Endothelial Histidine Decarboxylase Activity Following Exposure to Shearing Stresses," Exp. Mol. Pathol., **20**(3), pp. 329–343.
[4] Leung, D. Y., Glagov, S., and Mathews, M. B., 2003, "Cyclic Stretching Stimulates Synthesis of Matrix Components by Arterial Smooth Muscle Cells In Vitro," Science, **191**(4226), pp. 475–477.
[5] Haga, J. H., Li, Y. S., and Chien, S., 2007, "Molecular Basis of the Effects of Mechanical Stretch on Vascular Smooth Muscle Cells," J. Biomech., **40**(5), pp. 947–960.
[6] Davies, P. F., 2009, "Hemodynamic Shear Stress and the Endothelium in Cardiovascular Pathophysiology," Nat. Clin. Pract. Cardiovasc. Med., **6**(1), pp. 16–26.
[7] Wolinsky, H., and Glagov, S., 1967, "A Lamellar Unit of Aortic Medial Structure and Function in Mammals," Circ. Res., **20**(1), pp. 99–111.
[8] Shadwick, R. E., 1999, "Mechanical Design in Arteries," J. Exp. Biol., **202**(Pt. 23), pp. 3305–3313.
[9] Humphrey, J. D., 2008, "Vascular Adaptation and Mechanical Homeostasis at Tissue, Cellular, and Sub-Cellular Levels," Cell Biochem. Biophys., **50**(2), pp. 53–78.
[10] Fung, Y. C., 1967, "Elasticity of Soft Tissues in Simple Elongation," Am. J. Physiol., **213**(6), pp. 1532–1544.
[11] McEwen, W. K., and St Helen, R., 1965, "Rheology of the Human Sclera. Unifying Formulation of Ocular Rigidity," Ophthalmologica, **150**(5), pp. 321–346.
[12] Humphrey, J. D., 2002, *Cardiovascular Solid Mechanics: Cells, Tissues, and Organs*, Springer, NY.
[13] Chuong, C. J., and Fung, Y. C., 1986, "On Residual Stresses in Arteries," ASME J. Biomech. Eng., **108**(2), pp. 189–192.
[14] Bellini, C., Ferruzzi, J., Roccabianca, S., Di Martino, E. S., and Humphrey, J. D., 2014, "A Microstructurally Motivated Model of Arterial Wall Mechanics With Mechanobiological Implications," Ann. Biomed. Eng., **42**(3), pp. 488–502.
[15] Laurent, S., Boutouyrie, P., Asmar, R., Gautier, I., Laloux, B., Guize, L., Ducimetiere, P., and Benetos, A., 2001, "Aortic Stiffness Is an Independent Predictor of All-Cause and Cardiovascular Mortality in Hypertensive Patients," Hypertension, **37**(5), pp. 1236–1241.
[16] Laurent, S., Cockcroft, J., Van Bortel, L., Boutouyrie, P., Giannattasio, C., Hayoz, D., Pannier, B., Vlachopoulos, C., Wilkinson, I., Struijker-Boudier, H., and European Network for Non-Invasive Investigation of Large, A., 2006, "Expert Consensus Document on Arterial Stiffness: Methodological Issues and Clinical Applications," Eur. Heart J., **27**(21), pp. 2588–2605.
[17] McEniery, C. M., Yasmin, Hall, I. R., Qasem, A., Wilkinson, I. B., Cockcroft, J. R., and Investigators ACCT, 2005, "Normal Vascular Aging: Differential Effects on Wave Reflection and Aortic Pulse Wave Velocity: The Anglo-Cardiff Collaborative Trial (ACCT)," J. Am. Coll. Cardiol., **46**(9), pp. 1753–1760.
[18] Van Bortel, L. M., Laurent, S., Boutouyrie, P., Chowienczyk, P., Cruickshank, J. K., De Backer, T., Filipovsky, J., Huybrechts, S., Mattace-Raso, F. U., Protogerou, A. D., Schillaci, G., Segers, P., Vermeersch, S., Weber, T., and Artery, S., European Society of Hypertension Working Group on Vascular Function, and European Network for Noninvasive Investigation of Large Arteries, 2012, "Expert Consensus Document on the Measurement of Aortic Stiffness in Daily Practice Using Carotid-Femoral Pulse Wave Velocity," J. Hypertens., **30**(3), pp. 445–448.
[19] Laurent, S., and Boutouyrie, P., 2015, "The Structural Factor of Hypertension: Large and Small Artery Alterations," Circ. Res., **116**(6), pp. 1007–1021.
[20] Vinckier, A., and Semenza, G., 1998, "Measuring Elasticity of Biological Materials by Atomic Force Microscopy," FEBS Lett., **430**(1–2), pp. 12–16.
[21] Humphrey, J., Halperin, H. R., and Yin, F. C., 1991, "Small Indentation Superimposed on a Finite Equibiaxial Stretch. Implications for Cardiac Mechanics," ASME J. Appl. Mech., **58**(4), pp. 1108–1111.
[22] Costa, K. D., and Yin, F. C., 1999, "Analysis of Indentation: Implications for Measuring Mechanical Properties With Atomic Force Microscopy," ASME J. Biomech. Eng., **121**(5), pp. 462–471.
[23] Beatty, M., and Usmani, S., 1975, "On the Indentation of a Highly Elastic Half-Space," Q. J. Mech. Appl. Math., **28**(1), pp. 47–62.
[24] Na, S., Sun, Z., Meininger, G. A., and Humphrey, J. D., 2004, "On Atomic Force Microscopy and the Constitutive Behavior of Living Cells," Biomech. Model. Mechanobiol., **3**(2), pp. 75–84.
[25] Sehgel, N. L., Zhu, Y., Sun, Z., Trzeciakowski, J. P., Hong, Z., Hunter, W. C., Vatner, D. E., Meininger, G. A., and Vatner, S. F., 2013, "Increased Vascular Smooth Muscle Cell Stiffness: A Novel Mechanism for Aortic Stiffness in Hypertension," Am. J. Physiol. Heart Circ. Physiol., **305**(9), pp. H1281–H1287.
[26] Desai, A., Geraghty, S., and Dean, D., 2019, "Effects of Blocking Integrin Beta1 and N-Cadherin Cellular Interactions on Mechanical Properties of Vascular Smooth Muscle Cells," J. Biomech., **82**, pp. 337–345.
[27] Lindeman, J. H., Ashcroft, B. A., Beenakker, J. W., van Es, M., Koekkoek, N. B., Prins, F. A., Tielemans, J. F., Abdul-Hussien, H., Bank, R. A., and Oosterkamp, T. H., 2010, "Distinct Defects in Collagen Microarchitecture Underlie Vessel-Wall Failure in Advanced Abdominal Aneurysms and Aneurysms in Marfan Syndrome," Proc. Natl. Acad. Sci. U. S. A., **107**(2), pp. 862–865.
[28] Weisbrod, R. M., Shiang, T., Al Sayah, L., Fry, J. L., Bajpai, S., Reinhart-King, C. A., Lob, H. E., Santhanam, L., Mitchell, G., Cohen, R. A., and Seta, F., 2013, "Arterial Stiffening Precedes Systolic Hypertension in Diet-Induced Obesity," Hypertension, **62**(6), pp. 1105–1110.
[29] Liu, S. L., Bae, Y. H., Yu, C., Monslow, J., Hawthorne, E. A., Castagnino, P., Branchetti, E., Ferrari, G., Damrauer, S. M., Pure, E., and Assoian, R. K., 2015, "Matrix Metalloproteinase-12 Is an Essential Mediator of Acute and Chronic Arterial Stiffening," Sci. Rep., **5**, p. 17189.
[30] Lee, J. J., Galatioto, J., Rao, S., Ramirez, F., and Costa, K. D., 2016, "Losartan Attenuates Degradation of Aorta and Lung Tissue Micromechanics in a Mouse Model of Severe Marfan Syndrome," Ann. Biomed. Eng., **44**(10), pp. 2994–3006.
[31] Laurent, V. M., Hénon, S., Planus, E., Fodil, R., Balland, M., Isabey, D., and Gallet, FOIS., 2002, "Assessment of Mechanical Properties of Adherent Living Cells by Bead Micromanipulation: Comparison of Magnetic Twisting Cytometry Vs Optical Tweezers," ASME J. Biomech. Eng., **124**(4), pp. 408–421.
[32] Humphrey, J. D., and O'Rourke, S. L., 2015, *An Introduction to Biomechanics: Solids and Fluids, Analysis and Design*, Springer, New York.
[33] Zhu, W., Kim, B. C., Wang, M., Huang, J., Isak, A., Bexiga, N. M., Monticone, R., Ha, T., Lakatta, E. G., and An, S. S., 2018, "TGFβ1 Reinforces Arterial Aging in the Vascular Smooth Muscle Cell Through a Long-Range Regulation of the Cytoskeletal Stiffness," Sci. Rep., **8**(1), p. 2668.
[34] Cox, R. H., 1983, "Comparison of Arterial-Wall Mechanics Using Ring and Cylindrical Segments," Am. J. Physiol., **244**(2), pp. H298–H303.
[35] Baek, S., Gleason, R., Rajagopal, K., and Humphrey, J., 2007, "Theory of Small on Large: Potential Utility in Computations of Fluid–Solid Interactions in Arteries," Comput. Methods Appl. Mech. Eng., **196**(31–32), pp. 3070–3078.
[36] Holzapfel, G. A., and Ogden, R. W., 2010, "Constitutive Modelling of Arteries," Proc. R. Soc. A, **466**(2118), pp. 1551–1597.
[37] Schroeder, F., Polzer, S., Slazansky, M., Man, V., and Skacel, P., 2018, "Predictive Capabilities of Various Constitutive Models for Arterial Tissue," J. Mech. Behav. Biomed. Mater., **78**, pp. 369–380.
[38] Ferruzzi, J., Bersi, M. R., and Humphrey, J. D., 2013, "Biomechanical Phenotyping of Central Arteries in Health and Disease: Advantages of and Methods for Murine Models," Ann. Biomed. Eng., **41**(7), pp. 1311–1330.
[39] Humphrey, J. D., Harrison, D. G., Figueroa, C. A., Lacolley, P., and Laurent, S., 2016, "Central Artery Stiffness in Hypertension and Aging: A Problem With Cause and Consequence," Circ. Res., **118**(3), pp. 379–381.
[40] Humphrey, J. D., and Na, S., 2002, "Elastodynamics and Arterial Wall Stress," Ann. Biomed. Eng., **30**(4), pp. 509–523.
[41] Hodis, S., and Zamir, M., 2011, "Pulse Wave Velocity as a Diagnostic Index: The Pitfalls of Tethering Versus Stiffening of the Arterial Wall," J. Biomech., **44**(7), pp. 1367–1373.
[42] Learoyd, B. M., and Taylor, M. G., 1966, "Alterations With Age in the Viscoelastic Properties of Human Arterial Walls," Circ. Res., **18**(3), pp. 278–292.
[43] Lichtenstein, O., Safar, M. E., Mathieu, E., Poitevin, P., and Levy, B. I., 1998, "Static and Dynamic Mechanical Properties of the Carotid Artery From Normotensive and Hypertensive Rats," Hypertension, **32**(2), pp. 346–350.
[44] Farzaneh, S., Trabelsi, O., and Avril, S., 2019, "Inverse Identification of Local Stiffness Across Ascending Thoracic Aortic Aneurysms," Biomech. Model. Mechanobiol., **18**(1), pp. 137–153.
[45] Bersi, M. R., Bellini, C., Humphrey, J. D., and Avril, S., 2019, "Local Variations in Material and Structural Properties Characterize Murine Thoracic Aortic Aneurysm Mechanics," Biomech. Model. Mechanobiol., **18**(1), pp. 203–218.
[46] Holzapfel, G. A., 2006, "Determination of Material Models for Arterial Walls From Uniaxial Extension Tests and Histological Structure," J. Theor. Biol., **238**(2), pp. 290–302.
[47] Caulk, A. W., Humphrey, J., and Murtada, S. I., 2019, "Fundamental Roles of Axial Stretch in Isometric and Isobaric Evaluations of Vascular Contractility," ASME J. Biomech. Eng., **141**(3), pp. 031008.
[48] Humphrey, J. D., Eberth, J. F., Dye, W. W., and Gleason, R. L., 2009, "Fundamental Role of Axial Stress in Compensatory Adaptations by Arteries," J. Biomech., **42**(1), pp. 1–8.
[49] Vande Geest, J. P., Sacks, M. S., and Vorp, D. A., 2004, "Age Dependency of the Biaxial Biomechanical Behavior of Human Abdominal Aorta," ASME J. Biomech. Eng., **126**(6), pp. 815–822.
[50] Nagai, Y., Fleg, J. L., Kemper, M. K., Rywik, T. M., Earley, C. J., and Metter, E. J., 1999, "Carotid Arterial Stiffness as a Surrogate for Aortic Stiffness: Relationship Between Carotid Artery Pressure-Strain Elastic Modulus and Aortic Pulse Wave Velocity," Ultrasound Med. Biol., **25**(2), pp. 181–188.
[51] Bramwell, J. C., McDowall, R. J. S., and McSwiney, B. A., 1923, "The Variation of Arterial Elasticity With Blood Pressure in Man (Part I)," Proc. R. Soc. Lond. B. Biol. Sci., **94**(663), pp. 450–454.
[52] Spronck, B., Heusinkveld, M. H., Vanmolkot, F. H., Roodt, J. O., Hermeling, E., Delhaas, T., Kroon, A. A., and Reesink, K. D., 2015, "Pressure-Dependence of Arterial Stiffness: Potential Clinical Implications," J. Hypertens., **33**(2), pp. 330–338.
[53] Spronck, B., Delhaas, T., Butlin, M., Reesink, K. D., and Avolio, A. P., 2017, "Options for Dealing With Pressure Dependence of Pulse Wave Velocity as a Measure of Arterial Stiffness: An Update of Cardio-Ankle Vascular Index (CAVI) and CAVI0," Pulse, **5**(1–4), pp. 106–114.
[54] Shirai, K., Song, M., Suzuki, J., Kurosu, T., Oyama, T., Nagayama, D., Miyashita, Y., Yamamura, S., and Takahashi, M., 2011, "Contradictory Effects of Beta1- and Alpha1- Aderenergic Receptor Blockers on Cardio-Ankle Vascular Stiffness Index (CAVI)–CAVI Independent of Blood Pressure Computer Methods and Programs in Biomedicinere," J. Atheroscler. Thromb., **18**(1), pp. 49–55.
[55] Hayashi, K., Handa, H., Nagasawa, S., Okumura, A., and Moritake, K., 1980, "Stiffness and Elastic Behavior of Human Intracranial and Extracranial Arteries," J. Biomech., **13**(2), pp. 175–184.

[56] Spronck, B., Avolio, A. P., Tan, I., Butlin, M., Reesink, K. D., and Delhaas, T., 2017, "Arterial Stiffness Index Beta and Cardio-Ankle Vascular Index Inherently Depend on Blood Pressure But Can Be Readily Corrected," J. Hypertens., **35**(1), pp. 98–104.
[57] Xiao, N., Alastruey, J., and Alberto Figueroa, C., 2014, "A Systematic Comparison Between 1-D and 3-D Hemodynamics in Compliant Arterial Models," Int. J. Numer. Meth. Bio., **30**(2), pp. 204–231.
[58] Cuomo, F., Ferruzzi, J., Agarwal, P., Li, C., Zhuang, Z. W., Humphrey, J. D., and Figueroa, C. A., 2019, "Sex-Dependent Differences in Central Artery Haemodynamics in Normal and Fibulin-5 Deficient Mice: Implications for Ageing," Proc. R. Soc. A, **475**(2221), p. 20180076.
[59] Demiray, H., 1992, "Wave Propagation Through a Viscous Fluid Contained in a Prestressed Thin Elastic Tube," Int. J. Eng. Sci., **30**(11), pp. 1607–1620.
[60] Chuong, C. J., and Fung, Y. C., 1984, "Compressibility and Constitutive Equation of Arterial Wall in Radial Compression Experiments," J. Biomech., **17**(1), pp. 35–40.
[61] Hayenga, H. N., Trache, A., Trzeciakowski, J., and Humphrey, J. D., 2011, "Regional Atherosclerotic Plaque Properties in ApoE-/- Mice Quantified by Atomic Force, Immunofluorescence, and Light Microscopy," J. Vasc. Res., **48**(6), pp. 495–504.
[62] Leloup, A. J., Van Hove, C. E., Kurdi, A., De Moudt, S., Martinet, W., De Meyer, G. R., Schrijvers, D. M., De Keulenaer, G. W., and Fransen, P., 2016, "A Novel Set-Up for the Ex Vivo Analysis of Mechanical Properties of Mouse Aortic Segments Stretched at Physiological Pressure and Frequency," J. Physiol., **594**(21), pp. 6105–6115.
[63] Boutouyrie, P., Bećzie, Y., Lacolley, P., Challande, P., Chamiot-Clerc, P., Benetos, A., Renaud de la Faverie, J. F., Safar, M., and Laurent, S., 1997, "In Vivo/In Vitro Comparison of Rat Abdominal Aorta Wall Viscosity. Influence of Endothelial Function," Arterioscler. Thromb. Vasc. Biol., **17**(7), pp. 1346–1355.
[64] Bellini, C., Caulk, A. W., Li, G., Tellides, G., and Humphrey, J. D., 2017, "Biomechanical Phenotyping of the Murine Aorta: What Is the Best Control?" ASME J. Biomech. Eng., **139**(4), p. 044501.
[65] Haskett, D., Speicher, E., Fouts, M., Larson, D., Azhar, M., Utzinger, U., and Vande Geest, J., 2012, "The Effects of Angiotensin II on the Coupled Microstructural and Biomechanical Response of C57BL/6 Mouse Aorta," J. Biomech., **45**(5), pp. 772–779.
[66] Leloup, A. J., Fransen, P., Van Hove, C. E., Demolder, M., De Keulenaer, G. W., and Schrijvers, D. M., 2014, "Applanation Tonometry in Mice: A Novel Noninvasive Technique to Assess Pulse Wave Velocity and Arterial Stiffness," Hypertension, **64**(1), pp. 195–200.
[67] Fujikura, K., Luo, J., Gamarnik, V., Pernot, M., Fukumoto, R., Tilson, M. D., 3rd, and Konofagou, E. E., 2007, "A Novel Noninvasive Technique for Pulse-Wave Imaging and Characterization of Clinically-Significant Vascular Mechanical Properties In Vivo," Ultrason. Imaging, **29**(3), pp. 137–154.
[68] Trachet, B., Fraga-Silva, R. A., Londono, F. J., Swillens, A., Stergiopulos, N., and Segers, P., 2015, "Performance Comparison of Ultrasound-Based Methods to Assess Aortic Diameter and Stiffness in Normal and Aneurysmal Mice," PLoS One, **10**(5), p. e0129007.
[69] Saphirstein, R. J., and Morgan, K. G., 2014, "The Contribution of Vascular Smooth Muscle to Aortic Stiffness Across Length Scales," Microcirculation, **21**(3), pp. 201–207.
[70] Swift, J., Ivanovska, I. L., Buxboim, A., Harada, T., Dingal, P. C., Pinter, J., Pajerowski, J. D., Spinler, K. R., Shin, J. W., Tewari, M., Rehfeldt, F., Speicher, D. W., and Discher, D. E., 2013, "Nuclear Lamin-A Scales With Tissue Stiffness and Enhances Matrix-Directed Differentiation," Science, **341**(6149), p. 1240104.
[71] Truesdell, C., and Noll, W., 1965, *The Non-Linear Field Theories of Mechanics*, Springer, New York.
[72] Fung, Y. C., 1973, "Biorheology of Soft Tissues," Biorheology, **10**(2), pp. 139–155.
[73] Dajnowiec, D., and Langille, B. L., 2007, "Arterial Adaptations to Chronic Changes in Haemodynamic Function: Coupling Vasomotor Tone to Structural Remodelling," Clin. Sci., **113**(1), pp. 15–23.
[74] Humphrey, J. D., 2001, "Stress, Strain, and Mechanotransduction in Cells," ASME J. Biomech. Eng., **123**(6), pp. 638–641.
[75] Bersi, M. R., Ferruzzi, J., Eberth, J. F., Gleason, R. L., Jr., and Humphrey, J. D., 2014, "Consistent Biomechanical Phenotyping of Common Carotid Arteries From Seven Genetic, Pharmacological, and Surgical Mouse Models," Ann. Biomed. Eng., **42**(6), pp. 1207–1223.
[76] Humphrey, J. D., Dufresne, E. R., and Schwartz, M. A., 2014, "Mechanotransduction and Extracellular Matrix Homeostasis," Nat. Rev. Mol. Cell Biol., **15**(12), pp. 802–812.
[77] Greve, J. M., Les, A. S., Tang, B. T., Draney Blomme, M. T., Wilson, N. M., Dalman, R. L., Pelc, N. J., and Taylor, C. A., 2006, "Allometric Scaling of Wall Shear Stress From Mice to Humans: Quantification Using Cine Phase-Contrast MRI and Computational Fluid Dynamics," Am. J. Physiol. Heart Circ. Physiol., **291**(4), pp. H1700–H1708.
[78] Fung, Y., 2002, "Celebrating the Inauguration of the Journal: Biomechanics and Modeling in Mechanobiology," Biomech. Model. Mechanobiol., **1**(1), pp. 3–4.
[79] Green, A. E., and Adkins, J. E., 1970, *Large Elastic Deformations and Non-Linear Continuum Mechanics*, Clarendon Press, Oxford, UK.
[80] Oden, J., 1972, *Finite Elements of Nonlinear Continua*, McGraw-Hill, New York.